Chapter 3

Elastic modeling in discontinuous media

An essential part of elastic reverse-time migration involves the forward and backward time propagation of elastic wavefields. For schemes implemented in the space-time domain the time propagation is obtained by a numerical solution of the wave equation, usually by finite-difference or finite-element modeling methods. When the goal of the migration algorithm goes beyond the structural imaging of the subsurface, a dynamically accurate modeling scheme must be used. This chapter describes a modified high-order finite-difference modeling method whose dynamic response is more accurate than traditional finite-difference methods when the stiffness tensor model is discontinuous. The method produces stable, accurate results for both solid and liquid layers.

3.1   Introduction

Some important aspects of accurate finite-difference elastic modeling algorithms are the use of high-order differential operators, staggered grid computations, and a two-step implementation of the spatial operator by first obtaining the strains and then the stresses (Virieux, 1984, Dablain, 1986; Mora, 1986; Etgen, 1989). The high-order operators are required to avoid numerical anisotropy and dispersion, while the staggered scheme is important to allow the use of more accurate and stable operators, which have an even number of points, in a spatially synchronized way. One problem with these schemes is the lack of distinction between model and wavefield properties. The same differential operators are

applied to the components of the wavefield and to the components of the stiffness tensor. This is appropriate for smooth models but, whenever the subsurface geology is better described (within the resolution wavelength of the data) by a layered model with sharp interfaces, two-point operators are more suitable than large operators for computing the derivatives of the elastic parameters of the model.

The method developed here observes this important distinction by completely decoupling the computation of stiffness derivatives from the computation of wavefield derivatives. In addition, the discretization process uses the equivalence relations defined in the algebra of Shoenberg and Muir (1989), and a modified version of the conventional staggered grid introduced in wave-equation modeling by Virieux (1984; 1986). The method is efficiently implemented on a parallel platform. To test the method I compare the resulting wavefields with the analytical solution and with the results from other elastic modeling schemes.

3.2 The modeling operator

The elastic wave propagation modeling problem can be defined in the following way: find the particle displacement field $u(r, t)$ for all time t and at all spatial positions r inside a region $\mathcal{V}$, subjected to known boundary conditions $u(r_0, t)$ and $\dot{u}(r_0, t)$ at all points r_0 of $\mathcal{S}$, the boundary surface of $\mathcal{V}$, and known volumetric body forces (sources) $f(r, t)$ inside the region $\mathcal{V}$. The solution obeys the elastic wave equation, which can be expressed in its most general form as

$$\frac{\partial^2}{\partial t^2} u(r, t) = L(r) [u(r, t)] + f(r, t), \tag{3.1}$$

where $L(r)$ is a second-order linear differential operator of rank two, which depends on the stiffness tensor $C(r)$ and density $\rho(r)$ of the medium.

The method described in this chapter addresses the particular cases in which the region $\mathcal{V}$ is a rectangle in a two-dimensional space, and the medium has transverse-isotropic symmetry with a vertical axis of symmetry. Although substantially more expensive, generalization to three-dimensional space and general monoclinic symmetry is a straightforward process. For reasons that will become clear I will refer to this method as the dual-operator method.

3.2.1 Finite differences in discontinuous media?

Finite differences solutions of equation (3.1) involve the evaluation of the righthand side in a discrete grid, and numerical integration of the resulting equation using a finite time interval. Most methods of evaluating $\mathbf{L}\,\mathbf{u}$ do not make the important distinction between differentiation of media properties (enclosed in $\mathbf{L}$) and differentiation of the wavefield ($\mathbf{u}$). While the first will be in most cases a continuous function, the later will be only piecewise continuous for most realistic earth models.

The differential operator $\mathbf{L(r)}$ imposes continuity on the solution $\mathbf{u(r,}t)$ as well as any of its spatial derivatives, which translates to the physical constraints of stress and strain continuity. Several authors (Alford et al., 1974; Marfurt, 1984; Dablain, 1986) have discussed the problems of stability and accuracy in the numerical evaluation of the spatial and temporal derivatives of (3.1) in a discrete grid implementation. Producing stable and accurate estimations depends on several factors such as grid space and shape, time interval, elastic parameters, source spectrum, and operator size. However, all these analyses are based on the assumption that the object function is a discrete representation of a continuous function, that is, that the differencing function has "some degree" of smoothness. This restriction is clearly valid for the wavefield $\mathbf{u}$ in solid media, but is not valid for $\mathbf{u}$ if a fluid is present in $\mathcal{V}$, or for the derivatives involving C for the general case of discontinuous media.

To overcome this problem, the spatial derivatives of the wavefield and model parameters are evaluated by the dual-operator method with two distinct operators (Figure 3.1). The long, eighth-order wavefield differentiator is appropriate for accurately computing the derivative of a continuous function, while the short, second-order model differentiator is more suitable for piecewise continuous functions. Figure 3.2 illustrates the advantage of using the short operator at the model discontinuities.

Although it does not make sense to differentiate a discontinuous function at the point of discontinuity (unless we use one-sided operators with opposed symmetry at each side of the discontinuity), it is always possible to approximate the discontinuity by a steep linear transition zone. In this sense, the short operator gives a more accurate estimation of the derivative than the long operator, as can be confirmed by Figure 3.3, which represents the integration of the two derivatives shown in Figure 3.2.

FIG. 3.1. The two spatial derivative operators used in the discrete evaluation of **L u**.
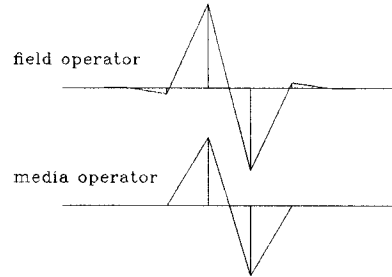
field operator

media operator

FIG. 3.2. (a) A discontinuous function. (b) Its derivative, as estimated by the long operator in Figure 3.1, and (c) its derivative, as estimated by the short operator in Figure 3.1.
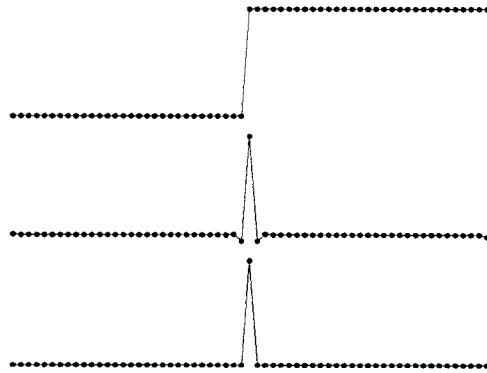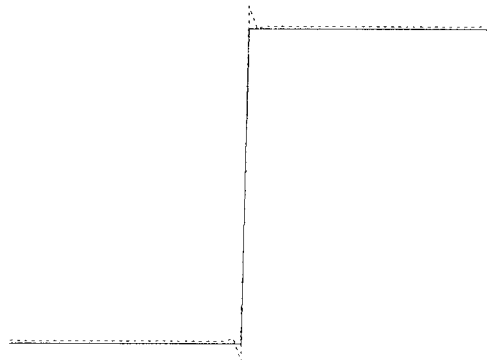
FIG. 3.3. The **continuous line** represents the integration of the derivative function shown in Figure 3.2c (short operator), while the **dashed-line** represents the integration of the derivative function shown in Figure 3.2b (long operator).

3.2.2 A modified staggered grid

Derivatives estimated with first-order antisymmetric differential operators are positioned at the gridpoints if the operator has an odd number of points and half-way between the gridpoints if the operator has an even number of points. Though easier to implement, the former operator becomes increasingly less accurate as the spatial frequency increases. Figure 3.4 compares the spectra of two high-order derivative operators, one having an even, one an odd number of points, with the "ideal spectrum" of the derivative operator (κ_x). No matter how many points it has, the odd-number operator always has a zero at Nyquist, which results in more dispersive and less stable algorithms.
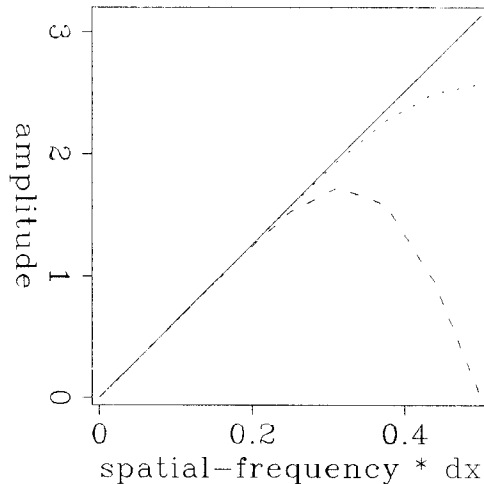
FIG. 3.4. The **continuous** line represents the ideal spectrum of the derivative operator (κ_x), the **dotted** line is the spectrum of an eight-point discrete operator, and the **dashed**-line is the spectrum of a nine-point discrete operator.

The traditional staggered grid for wave-equation modeling, which was introduced by Virieux (1984; 1986), has not only the horizontal and vertical components of the displacement field (as well as strains and stresses) evaluated at distinct (staggered) positions in space, but also distinct positions for the definition of different components of the stiffness tensor. The evaluation of **Lu** in this traditional staggered grid is implemented in two steps: first the strains are computed at intermediary positions and multiplied by the stiffnesses to obtain the stresses; then accelerations are obtained at the displacement positions by differentiating the stresses. One step uses a forward operator (the result is shifted forward by half a gridpoint), while the other uses a backward operator, so that the resulting acceleration has no net shift.

Figure 3.5 shows the modified staggered grid used to evaluate **Lu** in the dual-operator

method. In this figure x and z denote, respectively, the positions where the horizontal and vertical components of the displacement field are sampled, while all the components of the stiffness tensor C_{LM} (in condensed terminology) are defined at the same positions $C^{i,j}$.
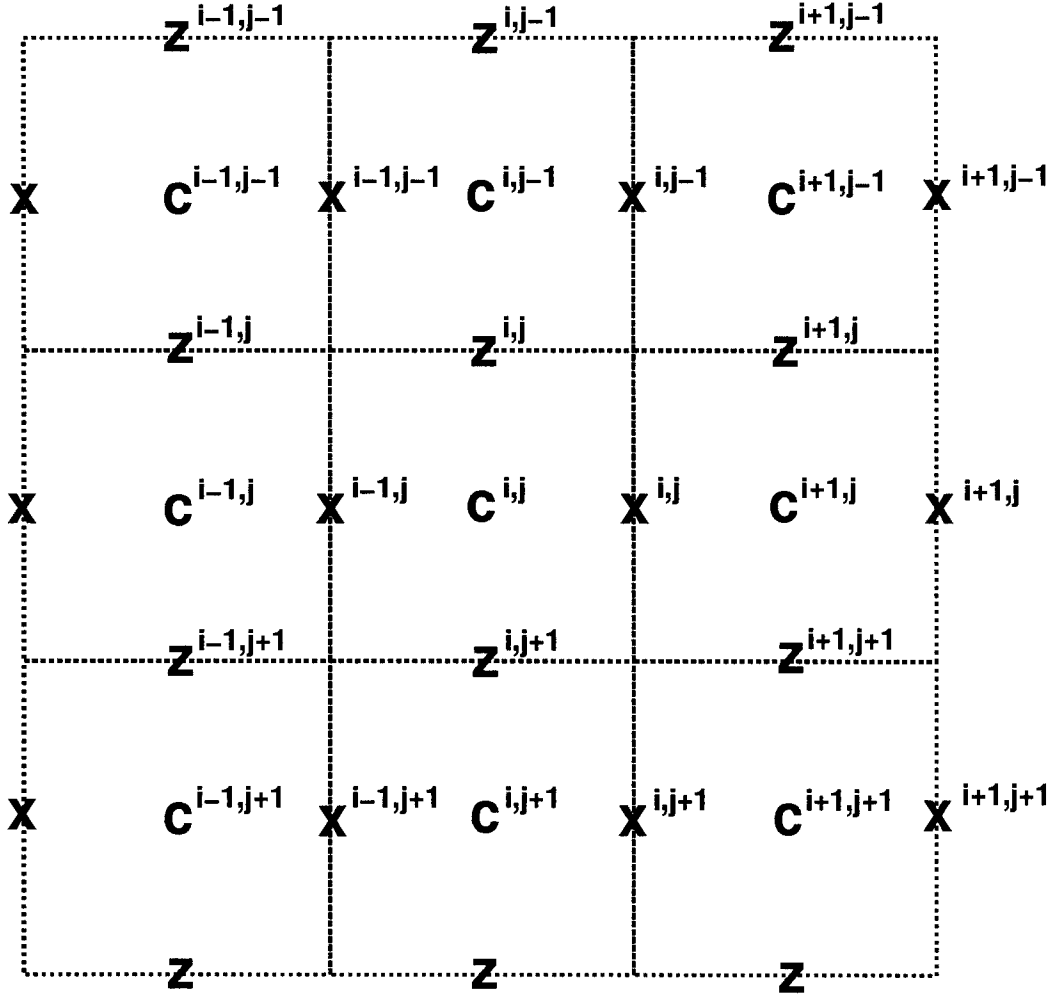

FIG. 3.5. Staggered grid used in the discrete implementation of the spatial operator $\mathbf{L(r)}$.

These changes in the staggered grid are necessary to implement the dual-operator scheme with even-number operators in a spatially synchronized way, but they also have an intrinsic advantage over the traditional staggered grid. The location of the Horizontal interfaces coincide with the gridpoints where the vertical displacements are defined while

the location of the vertical interfaces coincide with the gridpoints where the horizontal displacements are defined. This arrangement is particularly useful for solid-liquid interfaces, where the displacement component parallel to the interface is discontinuous.

3.2.3 Implementation of the spatial operator

In the discussion that follows *subscripts* refer to the components of tensors or vectors, while *superscripts* refer to their relative position in the grid.

Equation 3.1 can be rewritten in terms of the components of the vector wavefield **u** as

$$\rho \frac{\partial^2 u_i}{\partial t^2} = \frac{\partial \tau_{ij}}{\partial x_j} + f_i, \tag{3.2}$$

where indices i and j refer to the spatial components (x, y, z), f_i is the i component of the volumetric body forces, and τ_{ij} is the ij component of the stress field (Auld, 1990). In the 2-D transverse isotropic case (with vertical axis of symmetry), the x component of equation (3.2) becomes

$$\rho \frac{\partial^2 u_x}{\partial t^2} = \frac{\partial \tau_{xx}}{\partial x} + \frac{\partial \tau_{xz}}{\partial z} + f_i,$$

where

$$\tau_{xx} = c_{11} \frac{\partial u_x}{\partial x} + c_{13} \frac{\partial u_z}{\partial z}, \qquad \text{and} \qquad \tau_{xz} = c_{55} \left(\frac{\partial u_x}{\partial z} + \frac{\partial u_z}{\partial x} \right).$$

Combining these equations, and using the chain rule for the derivatives, we find for the x component

$$\rho \frac{\partial^2 u_x}{\partial t^2} = \frac{\partial c_{11}}{\partial x} \frac{\partial u_x}{\partial x} + c_{11} \frac{\partial^2 u_x}{\partial x^2} + \frac{\partial c_{13}}{\partial x} \frac{\partial u_z}{\partial z} + c_{13} \frac{\partial^2 u_z}{\partial x \partial z}$$
$$+ \frac{\partial c_{55}}{\partial z} \left(\frac{\partial u_x}{\partial z} + \frac{\partial u_z}{\partial x} \right) + c_{55} \left(\frac{\partial^2 u_x}{\partial z^2} + \frac{\partial^2 u_z}{\partial x \partial z} \right) + f_x, \tag{3.3}$$

and for the z component

$$\rho \frac{\partial^2 u_z}{\partial t^2} = \frac{\partial c_{33}}{\partial z} \frac{\partial u_z}{\partial z} + c_{33} \frac{\partial^2 u_z}{\partial z^2} + \frac{\partial c_{13}}{\partial z} \frac{\partial u_x}{\partial x} + c_{13} \frac{\partial^2 u_x}{\partial z \partial x}$$
$$+ \frac{\partial c_{55}}{\partial x} \left(\frac{\partial u_z}{\partial x} + \frac{\partial u_x}{\partial z} \right) + c_{55} \left(\frac{\partial^2 u_z}{\partial x^2} + \frac{\partial^2 u_x}{\partial z \partial x} \right) + f_z. \tag{3.4}$$

Contrary to the standard implementation of finite-difference algorithms, the differentiation of the model parameters is completely separated from the differentiation of the wavefield components, and since the model parameters do not change with time their derivatives need only be computed once.

To evaluate the righthand side of (3.3) and (3.4) it is necessary to use the notion of equivalent media to define the elastic parameters at intermediate points. The theoretical background is provided by the group theory of Shoenberg and Muir (1989), which defines the equations for finding the equivalent elastic parameters.

In the equations that follow, $\hat{c}$ and $\check{c}$ correspond to averaging in the horizontal direction

$$
\begin{aligned}
\hat{c}_{11}^{i,j} &= \frac{c_{11}^{i,j} + c_{11}^{i+1,j}}{2} \\
\hat{c}_{55}^{i,j} &= \frac{2\, c_{55}^{i,j}\, c_{55}^{i+1,j}}{c_{55}^{i,j} + c_{55}^{i+1,j}} \\
\check{c}_{55}^{i,j} &= \frac{c_{55}^{i,j} + c_{55}^{i+1,j}}{2} \\
\hat{c}_{13}^{i,j} &= \frac{\hat{c}_{11}^{i,j}}{2}\left(\frac{c_{13}^{i,j}}{c_{11}^{i,j}} + \frac{c_{13}^{i+1,j}}{c_{11}^{i+1,j}}\right),
\end{aligned}
\tag{3.5}
$$

which are all positioned between $c^{i,j}$ and $c^{i+1,j}$, while $\tilde{c}$ and $\bar{c}$ correspond to averaging in the vertical direction

$$
\begin{aligned}
\tilde{c}_{33}^{i,j} &= \frac{c_{33}^{i,j} + c_{33}^{i,j-1}}{2} \\
\tilde{c}_{55}^{i,j} &= \frac{2\, c_{55}^{i,j}\, c_{55}^{i,j-1}}{c_{55}^{i,j} + c_{55}^{i,j-1}} \\
\bar{c}_{55}^{i,j} &= \frac{c_{55}^{i,j} + c_{55}^{i,j-1}}{2} \\
\tilde{c}_{13}^{i,j} &= \frac{\tilde{c}_{33}^{i,j}}{2}\left(\frac{c_{13}^{i,j}}{c_{33}^{i,j}} + \frac{c_{13}^{i,j-1}}{c_{33}^{i,j-1}}\right),
\end{aligned}
\tag{3.6}
$$

which are all positioned between $c^{i,j}$ and $c^{i,j-1}$.

For the differential operator, the following convention applies: δ^+ and δ^- correspond, respectively, to the forward and backward *long* wavefield operators; Δ^+ and Δ^- correspond to the *short* model operators. Subscripts are used to distinguish horizontal and vertical derivatives. Following these conventions, the differential operators are defined as:

$$
\begin{aligned}
(\Delta_x^+ c_{11})^{i,j} &= c_{11}^{i+1,j} - c_{11}^{i,j} \\
(\Delta_x^+ c_{13})^{i,j} &= c_{13}^{i+1,j} - c_{13}^{i,j} \\
(\Delta_x^- c_{55})^{i,j} &= \frac{1}{2}(\hat{c}_{55}^{i,j} + \hat{c}_{55}^{i,j-1} - \hat{c}_{55}^{i-1,j} - \hat{c}_{55}^{i-1,j-1})
\end{aligned}
\tag{3.7}
$$

$$(\Delta_z^- c_{33})^{i,j} = c_{33}^{i,j} - c_{33}^{i,j-1}$$

$$(\Delta_z^- c_{13})^{i,j} = c_{13}^{i,j} - c_{13}^{i,j-1}$$

$$(\Delta_z^+ c_{55})^{i,j} = \frac{1}{2}(\tilde{c}_{55}^{i,j+1} + \tilde{c}_{55}^{i+1,j+1} - \tilde{c}_{55}^{i,j} - \tilde{c}_{55}^{i+1,j}),$$

and

$$\hat{\delta}_x = \frac{\delta_x^+ + \delta_x^-}{2}$$

$$\tilde{\delta}_z = \frac{\delta_z^+ + \delta_z^-}{2}$$

$$(\hat{\delta}_z^+)^{i,j} = \frac{(\delta_z^+)^{i,j} + (\delta_z^+)^{i+1,j}}{2}$$

$$(\hat{\delta}_z^-)^{i,j} = \frac{(\delta_z^-)^{i,j} + (\delta_z^-)^{i-1,j}}{2}$$

$$(\tilde{\delta}_x^+)^{i,j} = \frac{(\delta_x^+)^{i,j} + (\delta_x^+)^{i,j+1}}{2}$$

$$(\tilde{\delta}_x^-)^{i,j} = \frac{(\delta_x^-)^{i,j} + (\delta_x^-)^{i,j-1}}{2}.$$

Using these definitions, the spatial operator is given by

$$\mathbf{Lu} = \begin{bmatrix} L_{11} & L_{12} \\ L_{21} & L_{22} \end{bmatrix} \begin{pmatrix} u_x \\ u_z \end{pmatrix}, \tag{3.8}$$

where

$$L_{11} = \frac{\hat{c}_{11}\delta_x^+ \delta_x^- + (\Delta_x^+ c_{11})\delta_x^- + \check{c}_{55}\delta_z^+ \delta_z^-}{\rho(\Delta x)^2} +; \frac{(\Delta_z^+ c_{55})\tilde{\delta}_z}{\rho(\Delta z)^2}$$

$$L_{12} = \frac{(\hat{c}_{13} + \hat{c}_{55})\,\delta_x^+ \delta_z^+ + (\Delta_x^+ c_{13})\hat{\delta}_z^+ + (\Delta_z^+ c_{55})\tilde{\delta}_x^+}{\rho \Delta x \Delta z}$$

$$L_{22} = \frac{\tilde{c}_{33}\delta_z^+ \delta_z^- + (\Delta_z^- c_{33})\delta_z^+ + \bar{c}_{55}\delta_x^+ \delta_x^-}{\rho(\Delta z)^2} + \frac{(\Delta_x^- c_{55})\hat{\delta}_x}{\rho(\Delta x)^2}$$

$$L_{21} = \frac{(\tilde{c}_{13} + \tilde{c}_{55})\,\delta_z^- \delta_x^- + (\Delta_z^- c_{13})\tilde{\delta}_x^- + (\Delta_x^- c_{55})\hat{\delta}_z^-}{\rho \Delta x \Delta z}.$$

$$\tag{3.9}$$

3.2.4 Time propagation

Once **Lu** is evaluated there are many possible choices for the time integration of 3.1. The method presented here uses a time-propagation operator to update the particle displacement field and the particle velocity field from time t to time $t + dt$. For simplicity,

the source term is not included in the derivation of the operator. The basic principle is similar to the one used by Dablain (1986) to derive a fourth-order-in-time, explicit, finite-difference scheme. Contrary to the method presented here, Dablain's scheme used two time-step solutions ($u(t - \Delta t)$ and $u(t)$) in order to find $u(t + \Delta t)$.

Omitting the source term and taking successive time derivatives of the wave equation 3.1 leads to the following relations:

$$\frac{d^2 u(t)}{dt^2} = \mathbf{L}u(t), \qquad \frac{d^3 u(t)}{dt^3} = \frac{d^2 \dot{u}(t)}{dt^2} = \mathbf{L}\dot{u}(t), \qquad \frac{d^4 u(t)}{dt^4} = \mathbf{L}^2 u(t), \qquad \dots$$

These relations can be substituted in the Taylor expansions of $u(t + dt)$ around $u(t)$, and $\dot{u}(t + dt)$ around $\dot{u}(t)$, as follows:

$$u(t + dt) = u(t) + \dot{u}(t)dt + \frac{\mathbf{L}}{2}u(t)dt^2 + \frac{\mathbf{L}}{6}\dot{u}(t)dt^3 + \dots \qquad (3.10)$$

$$\dot{u}(t + dt) = \dot{u}(t) + \mathbf{L}u(t)dt + \frac{\mathbf{L}}{2}\dot{u}(t)dt^2 + \frac{\mathbf{L}^2}{6}u(t)dt^3 + \dots \; .$$

Combining these two equations, we obtain the time-propagation equation

$$\begin{pmatrix} u \\ \dot{u} \end{pmatrix}_{t+dt} \approx \mathbf{P}^+ \begin{pmatrix} u \\ \dot{u} \end{pmatrix}_t, \qquad \text{without source,} \qquad (3.11)$$

where the forward time-propagation operator $\mathbf{P}^+$ has the following form:

$$\mathbf{P}^+ = \begin{bmatrix} \mathbf{I} + \frac{\mathbf{L}}{2}dt^2 + \frac{\mathbf{L}^2}{24}dt^4 & \mathbf{I}dt + \frac{\mathbf{L}}{6}dt^3 \\ \mathbf{L}\left(\mathbf{I}dt + \frac{\mathbf{L}}{6}dt^3\right) & \mathbf{I} + \frac{\mathbf{L}}{2}dt^2 + \frac{\mathbf{L}^2}{24}dt^4 \end{bmatrix} \qquad (3.12)$$

for the specific case of a fourth-order approximation in time.

Keeping the source term in the previous derivation will introduce an additional term in 3.11, as follows:

$$\begin{pmatrix} u \\ \dot{u} \end{pmatrix}_{t+dt} \approx \mathbf{P}^+ \begin{pmatrix} u \\ \dot{u} \end{pmatrix}_t + \mathbf{A}\,\tilde{f}, \qquad \text{with source,} \qquad (3.13)$$

where $\mathbf{A}$ is an operator that depends only on powers of dt, and $\tilde{f} = (f, \dot{f}, \ddot{f}, \dots)$.

3.3 Boundary conditions

3.3.1 Absorbing boundaries

The absorbing boundary conditions in the sides and bottom of the model are based on the method described by Cerjan et al. (1985), which is both simple and suitable for

implementation on a parallel platform. An N-grid-points-thick absorbing region covers the three absorbing regions. Following each time step, the wavefield inside this region is multiplied by a Gaussian damping function $G = \exp{-[(N - i)/\sigma_N]^2}$., where i is the distance (in gridpoints units) from the boundary. The total attenuation applied to a wavefield propagating with an extreme velocity of one gridpoint per time-step is

$$\Psi(t + 2N\Delta t) = \prod_{i=1}^{N} G^2(i), \tag{3.14}$$

as illustrated in Figure 3.6. Stable modeling requires smaller velocities than that, resulting in a cumulative attenuation stronger than that described by equation (3.14). One of the nice things about the parallel architecture is the facility provided by the natural circular boundary conditions. No special treatment is required for the two sides of the model because the waves transmitted from one boundary to the other are sufficiently attenuated as to have no significant effect in the wavefield outside the boundary region.
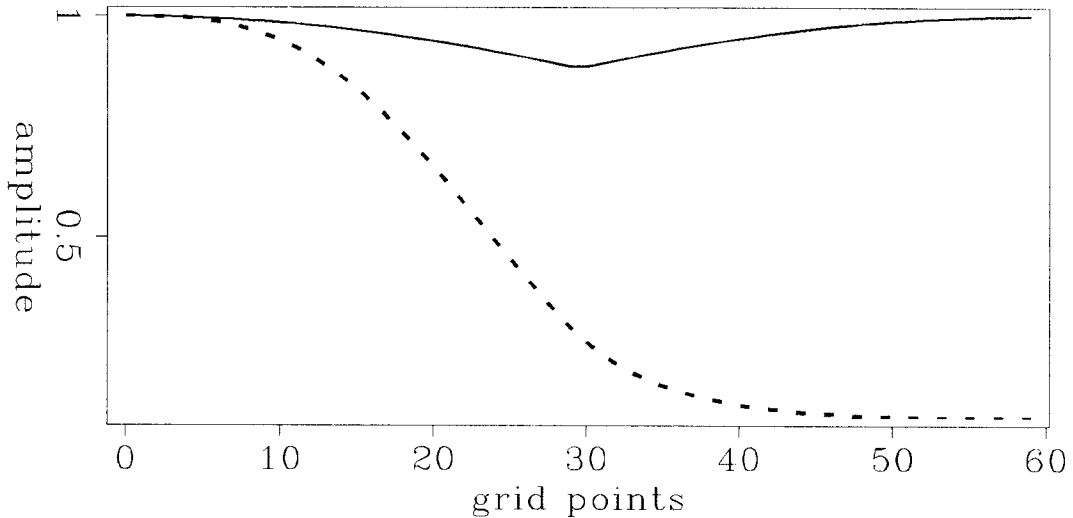

FIG. 3.6. The **continuous** curve represents the attenuation applied at each gridpoint inside the absorbing region, while the **dashed**-line represents the cumulative attenuation suffered by a wavefield propagating with a velocity of one gridpoint per time-step, as described by equation (3.14).

3.3.2 Free surface and the source term

The upper boundary is considered as a perfect mirror that simulates a free boundary condition. It is necessary to address two implementation issues in this simulation: how

to apply the spatial operators at gridpoints closer to the surface than the half-size of the operators, and how to define the source term.

When applied to the gridpoints near the surface, the spatial operators are folded back (reflected) in the following way: The part of the operator that operates in the vertical component of the wavefield retains its original polarity, while the part that operates in the horizontal component has its polarity reversed (see Figure 3.7a).
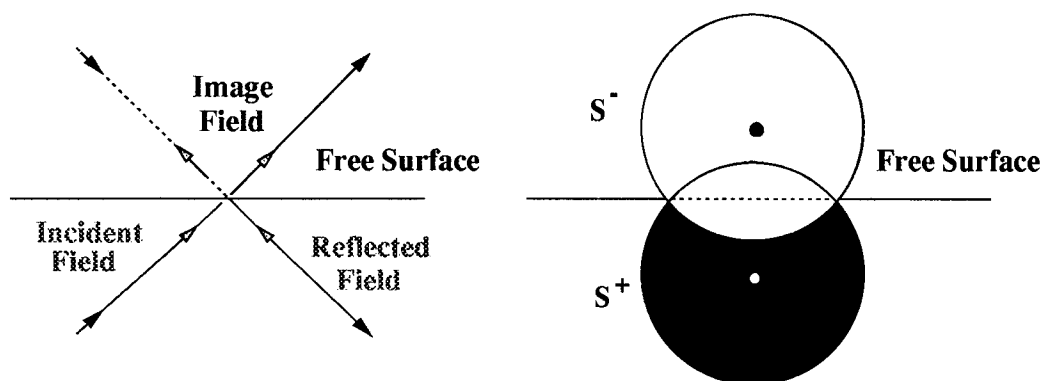

FIG. 3.7. The free-surface boundary can be replaced by an image medium and an image source. *(a)* The image wavefield has the same amplitude and reverse horizontal polarity as the object field. The black arrow represents the propagation direction; the white arrow, the polarization direction. *(b)* The image source also has reverse horizontal polarity and is effective in the modeling only if located sufficiently close to the boundary.

The source term is introduced as an additive contribution to the wavefield at the source location, during the time span in which the source is considered active. To avoid spatial aliasing (and also to allow the definition of a purely compressional source), the source needs to be spatially smooth, that is, covering only a small region of space (a few gridpoints). When the source is located sufficiently close to the surface (as is usually the case in the real world) the free-surface image of the source will be also active in the bottom space where the model is defined, as Figure 3.7b shows. Therefore, the source term needs to be introduced as the sum of the contributions of the *real* source and of its *image* in the model-space region.

### 3.3.3 Recorded fields near the surface

In the staggered grid implementation, the horizontal and vertical components of the displacement field are defined at different spatial positions. Because in most subsequent applications the wavefields are considered to be sampled at the same place, it is necessary

to spatially interpolate the components of the "recorded wavefield." The interpolation is performed with an eight-point operator that is applied vertically in the vertical component, and horizontally in the horizontal component, resulting in an interpolated vector field at the same locations at which the elastic parameters are defined. This and the other operators defined in this subsection are derived by solving a system of equations obtained from a set of Taylor expansions around the interpolating point.

Furthermore, if the "receivers" are located in a liquid layer (marine survey) it is desirable that a pressure wavefield be also generated for "recording." To accomplish this the algorithm first calculates the divergence of the wavefield and then applies equation (2.2). The resulting pressure field is also located at the same locations at which the elastic parameters are defined.

For practical applications the wavefield must be "recorded" at the gridpoints adjacent to the free surface. To allow this, the vertical interpolation of the vertical component, as well as the vertical derivative of the vertical component, must be evaluated with asymmetric operators, which are obtained in much the same way as symmetric ones. Figure 3.8 shows the four operators used in the interpolation and divergence of the wavefields at the surface boundary gridpoints.

FIG. 3.8. Interpolation and derivative operators used to obtain the recorded elastic wavefield and the pressure wavefield at the surface-boundary gridpoints.
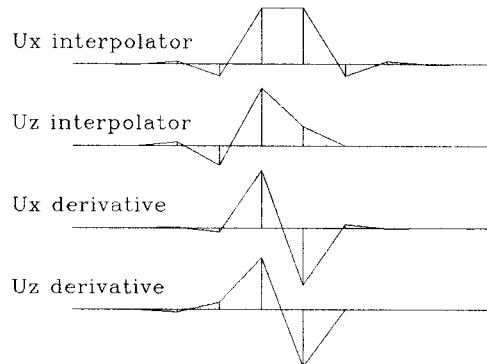
3.4 Dynamic behavior

The kinematics of the wavefield are not affected by the introduction of a short operator to compute the model derivatives nor by the use of equivalent medium theory in the evaluation of the spatial operator. I introduced these changes to better simulate the

dynamics of the wave-propagation problem. A simple model with horizontal layers was used to compare the dual-operator approach with a traditional finite-difference algorithm, and with an elastic modeling algorithm based on the Haskell-Thomson propagator-matrix method (Aki and Richards, 1980), which is restricted to horizontally-layered models. To test the stability and accuracy of these three schemes in extreme conditions, a water layer was placed at the top of the model.

Figure 3.9 describes the model parameters. Figure 3.10 shows the horizontal and vertical components of the wavefield generated by the dual-operator modeling scheme using the model of Figure 3.9. The reflections with zero-offset traveltime equal to 0.8, 1.1, and 1.55 seconds correspond, respectively, to the water-bottom reflection, the reflection in the interface between the second and third layers, and the first multiple of the water-bottom reflection. The two other visible reflections correspond to the PS and SS reflections at the interface between the second and third layers.
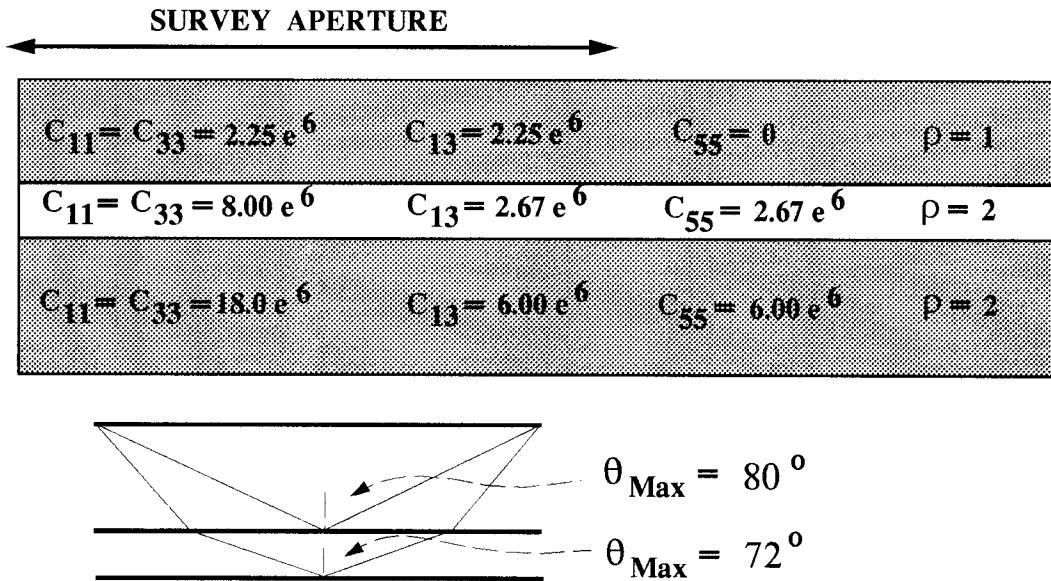
SURVEY APERTURE

$C_{11}= C_{33} = 2.25\,e^{6}$	$C_{13}= 2.25\,e^{6}$	$C_{55}= 0$	$\rho = 1$
$C_{11}= C_{33} = 8.00\,e^{6}$	$C_{13}= 2.67\,e^{6}$	$C_{55}= 2.67\,e^{6}$	$\rho = 2$
$C_{11}= C_{33} = 18.0\,e^{6}$	$C_{13}= 6.00\,e^{6}$	$C_{55}= 6.00\,e^{6}$	$\rho = 2$

$$\theta_{Max} = 80^{o}$$

$$\theta_{Max} = 72^{o}$$

FIG. 3.9. Model used to compare the results obtained with three different modeling schemes. Elastic constants are given in N/m^{2}, and densities in g/cm^{3}.

Figure 3.11 shows the vertical and horizontal components of the wavefield generated with the Haskell-Thomson scheme, and Figure 3.12 shows the vertical and horizontal components of the wavefield generated with the traditional finite-difference scheme.

The wavelet is clearly broader in both finite-difference-based methods because they require that the source extend over more than one gridpoint. That is also the reason
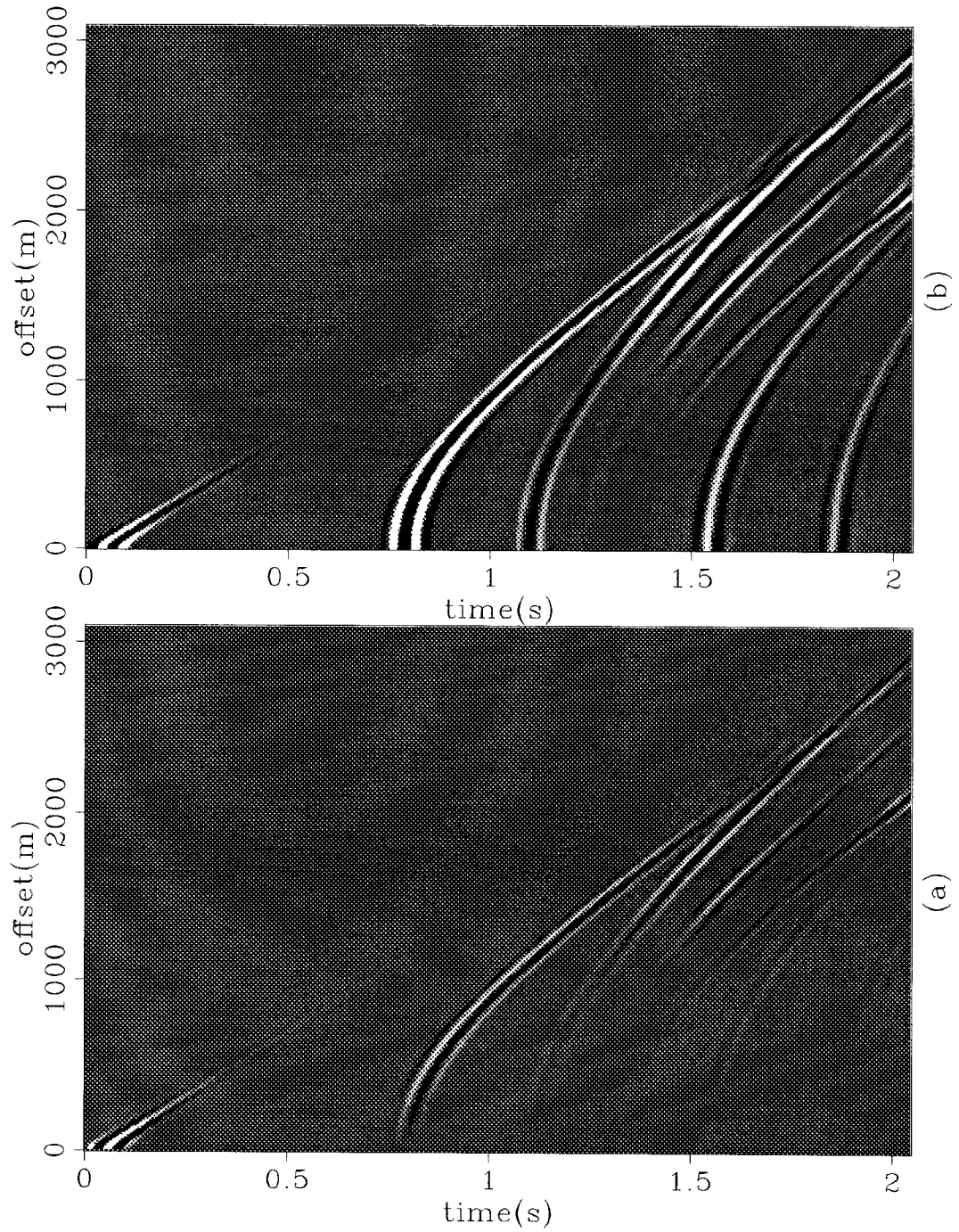
FIG. 3.10. Surface wavefield generated by the dual-operator scheme. (a) Horizontal component. (b) Vertical component.
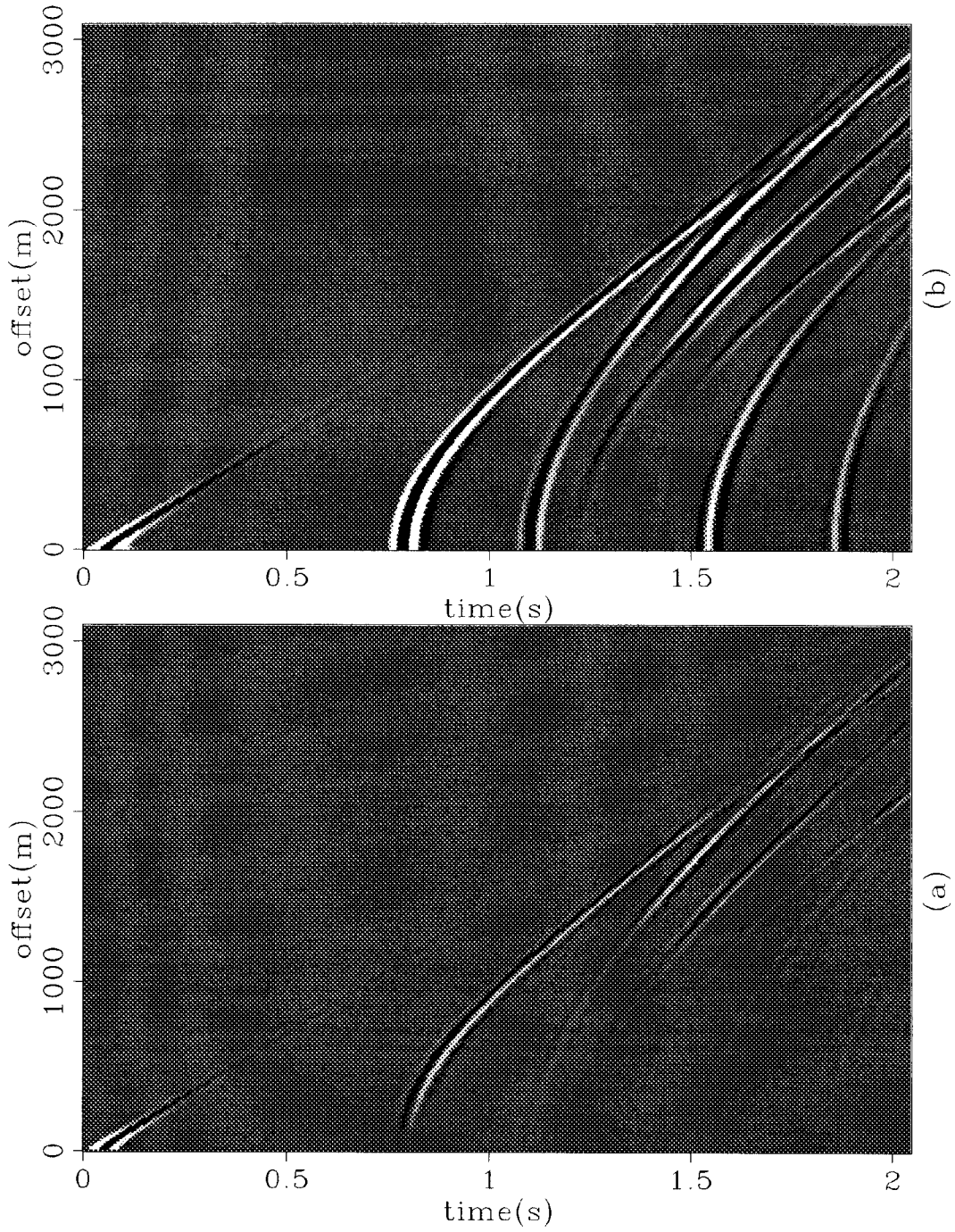
FIG. 3.11. Surface wavefield generated by the propagator-matrix scheme. (a) Horizontal component. (b) Vertical component.
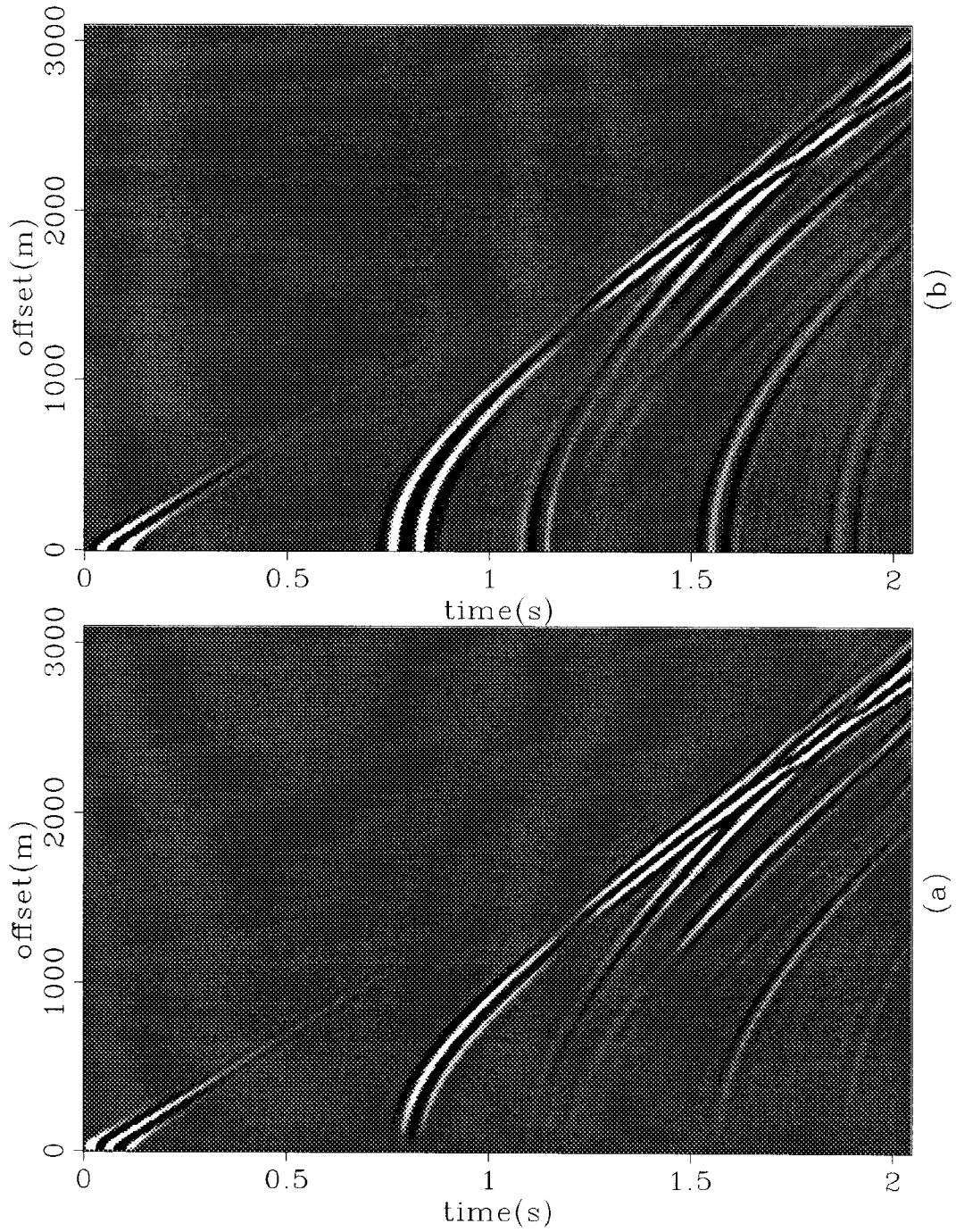
FIG. 3.12. Surface wavefield generated by the traditional finite-difference scheme. (a) Horizontal component. (b) Vertical component.

for the small precursor lobe in the wavelet generated by these two methods. Although both finite-difference schemes have operators with the same number of points (of same order in time and space), the traditional method is more dispersive, as indicated by the high-frequency ringing that contaminates the near traces of the vertical component. This higher dispersion is noticeable mainly when a liquid layer is present. Other differences are: the phase change of the sea bottom reflection near the offset 1300 meters in the vertical component of the traditional finite-difference scheme, the much weaker amplitude of the PSSP mode (the third event from the bottom) in the traditional finite-difference scheme, and the weaker near-offset amplitude of the PSPP mode (the fourth event from the bottom) in both finite-difference schemes relative to the propagator-matrix scheme. Some of these differences can also be observed in the tau-p domain representation of the displacement amplitude ($\mathrm{sgn}(u_z) \sqrt{u_x^2 + u_z^2}$) of the three datasets shown in Figure 3.14.

3.4.1   The zero-offset waveform

The first comparison involves the zero-offset response of the three methods. A window that includes the first two primary reflections (both PP) was selected from the zero-offset trace of the vertical components for the three simulated wavefields. Figure 3.13 shows the three waveforms. Except for small differences in the amplitude and the precursor lob, the waveforms generated by the propagator-matrix and dual-operator methods are very similar. The dispersion is minimal and the kinematics are in accordance with theoretical expectations. The dispersive character observed in the wavefield of the traditional finite-difference scheme becomes more clear in the selected window. As a result of the dispersion, the traveltime differences between the two reflections (using the central picks as the measuring criterion) is slightly larger than the theoretical value.

The theoretical ratio between the amplitudes of the two reflections is given by

$$\frac{\mathrm{Amp}_2}{\mathrm{Amp}_1} = \frac{R_2}{R_1}\,(1 - R_1^2)\left[\frac{t_1 v_1^2}{(t_2 - t_1)v_2^2 + t_1 v_1^2}\right]^{1/2},$$

where the first term is the ratio between the normal incidence reflection coefficients, the second term is the two-way transmission coefficient, and the third term is the 2D-divergence relative correction. The value obtained from the propagator-matrix trace coincides with the predicted value, while the value from the dual-operator trace is 3.7 percent higher, and the value from the traditional finite-difference trace is 7.5 percent lower.
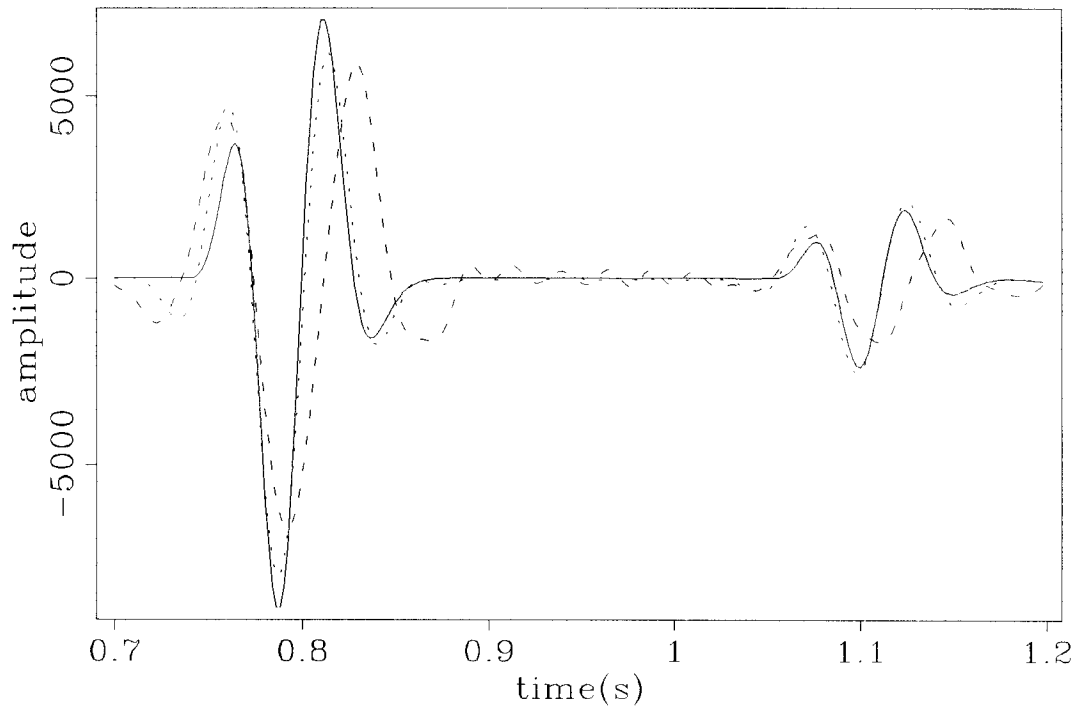
FIG. 3.13. Zero offset response generated by the three schemes. The three curves correspond to a window selected from the first traces of Figures 3.10a, 3.11a, and 3.12a, which includes the reflections from the first two interfaces of the model. The **continuous** line comes from the Haskell-Thomson scheme, the **dotted**-line comes from the dual-operator scheme, and the **dashed**-line comes from the traditional finite-difference scheme.

3.4.2 Amplitude versus offset

As important as the relative response between different reflections is the amplitude response of a single reflection as a function of the offset, or the illumination angle. The two P-to-P reflections of the previous subsection are separately analyzed here. To allow a direct comparison with the analytical curve for the PP plane-wave reflection coefficient, the wavefields simulated by each of the methods were mapped to the tau-p domain (Figure 3.14), which corresponds to the plane-wave decomposition of the original wavefields. Each figure used in this analysis contains five curves. The two continuous curves correspond to the real and imaginary parts of the theoretical P-to-P *plane-wave response* as a function of the horizontal slowness. The theoretical response includes the PP reflection coefficient and the two-way (angle-dependent) PP transmission coefficient. The other three curves come from the tau-p transform of the simulated wavefields, multiplied by a scaling factor that normalizes the amplitudes of the fifteenth horizontal-slowness sample to the theoretical amplitude of that sample. Figure 3.15 shows the analytical traveltime trajectories in the tau-p domain overlain the wavefields generated by the three schemes using a model without the second interface to avoid interference from crossing events. The contrast in the amplitude and phase behavior at the critical slowness (0.0005 seconds/meter), between the traditional finite-difference scheme and the other two schemes is apparent in this figure. The weak linear event observed in 3.15c comes from the abrupt amplitude change at the critical slowness.

Figure 3.16 shows the curves associated with the water-bottom reflection. In the low horizontal slowness region the dual-operator (dashed-line) and the propagator-matrix (dotted-line) curves fit the theoretical curve almost perfectly. The traditional finite-difference modeling (dashed-dotted-line) not only oscillates more than the other two curves but also has a reversed "AVO signature"; the amplitude increases with the horizontal-slowness. In the high horizontal slowness region, the traditional finite-difference method completely fails to approximate the theoretical curve while the other two methods still maintain a reasonably close fitting of the theoretical curve.

As in the previous case, the curves for the second PP primary reflection (Figure 3.17) approximate well the theoretical curve for low values of horizontal slowness. Again, the curve from the traditional finite-difference scheme is much more jagged than the curves from the other two schemes. For larger values of horizontal slowness, the dual-operator and the propagator-matrix curves are closer to the theoretical curve than the traditional
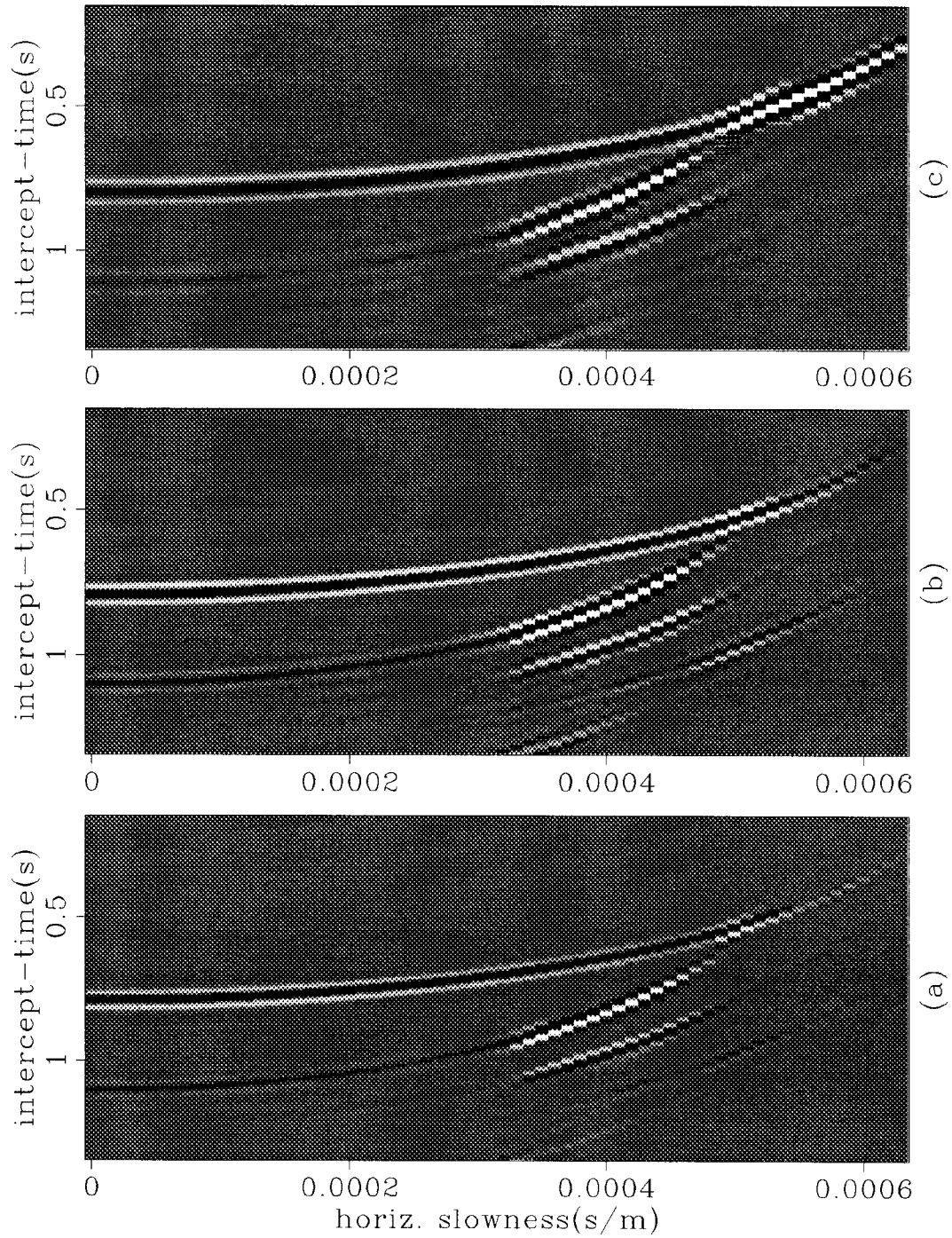
FIG. 3.14. Tau-p domain window of the displacement amplitude of the wavefield generated by: (a)the propagator-matrix scheme, (b) the dual-operator scheme, and (c) the traditional finite-difference scheme.
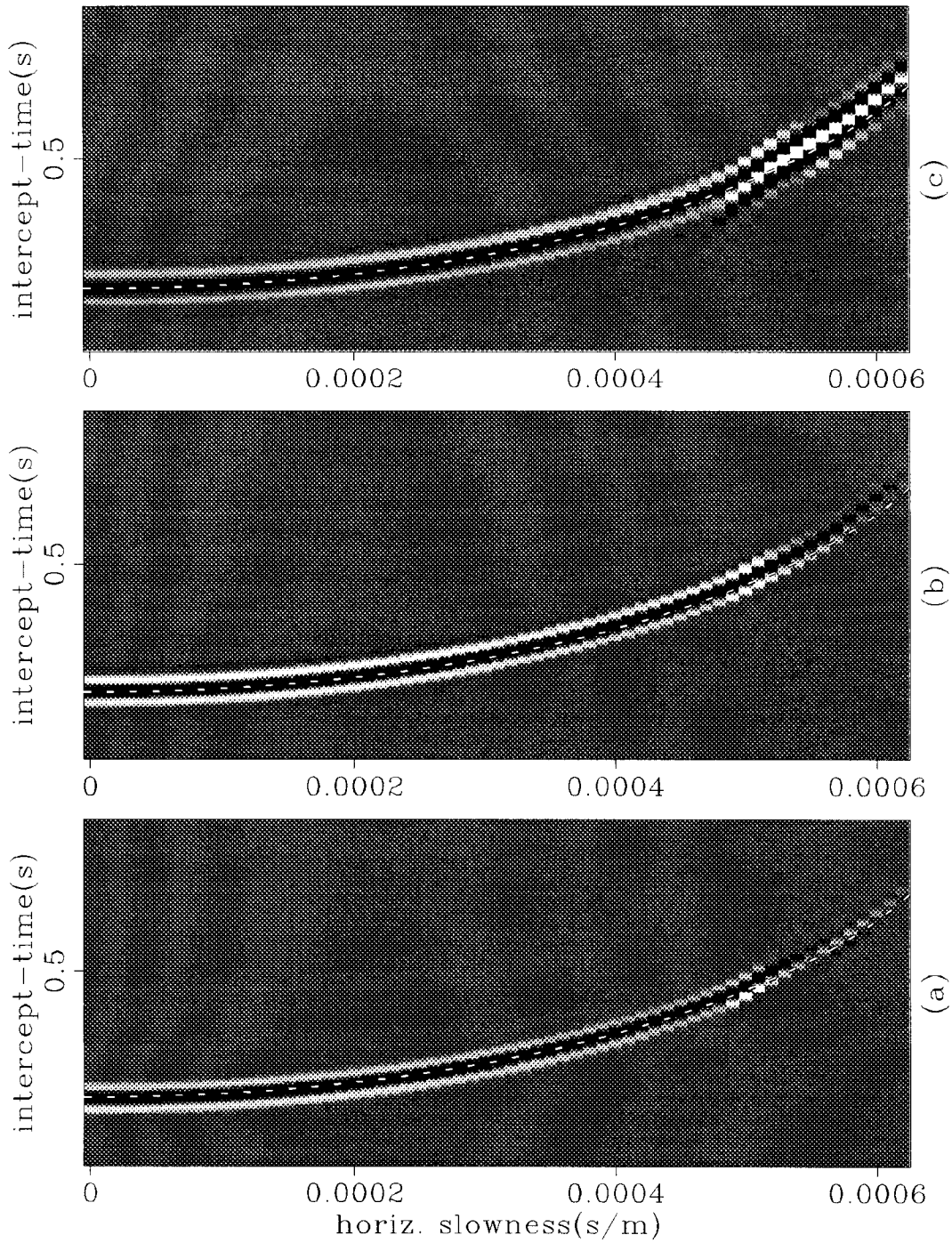
FIG. 3.15. Tau-p domain window of the displacement amplitude of the wavefield generated by: (a)the propagator-matrix scheme, (b) the dual-operator scheme, and (c) the traditional finite-difference scheme. The overlaid dashed curve is the analytical traveltime trajectory corresponding to the first interface.
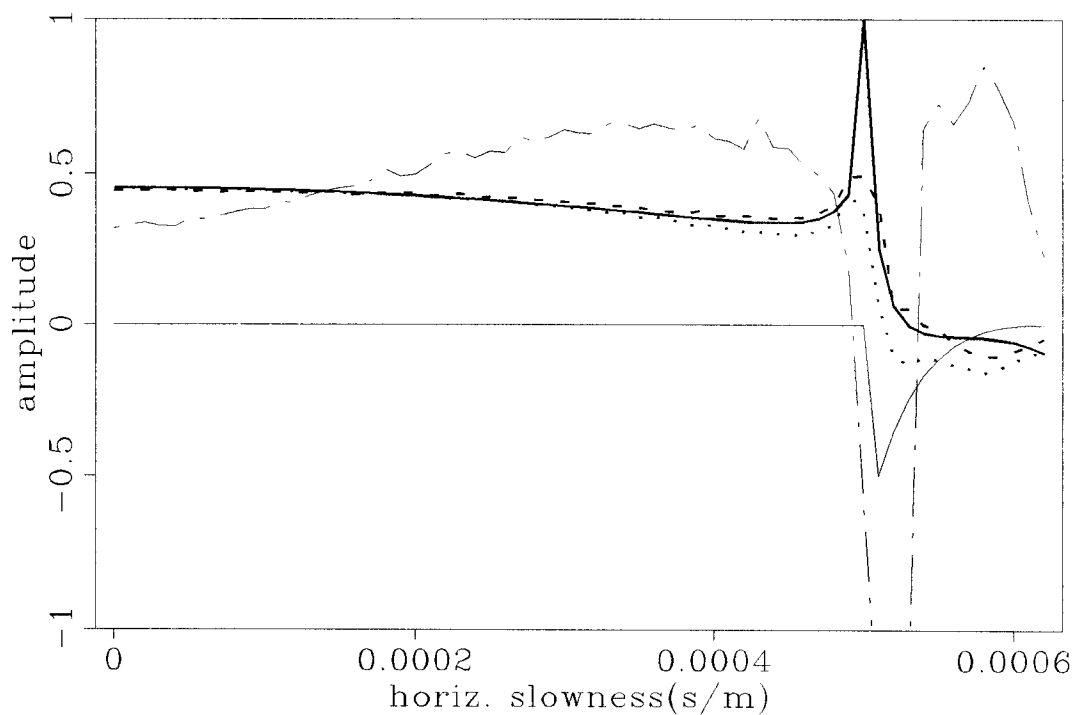
FIG. 3.16. Amplitude versus horizontal slowness of the PP reflection from the water-bottom interface. These curves were extracted from the plane-wave decomposition of the wavefields generated by the three modeling schemes. The **thick continuous** line and the **thin continuous** line correspond, respectively, to the real and imaginary parts of the theoretical PP plane-wave reflection coefficient; the **dotted**-line is the amplitude response from the propagator-matrix scheme; the **dashed**-line is the amplitude response from the dual-operator scheme; the **thin dot-dashed**-line comes from the traditional finite-difference scheme.

finite-difference curve with better fit than in the water bottom case, mainly because the interference with other events is much weaker in this case. Particularly impressive is the extremely good fitting obtained by the dual-operator method (dashed-line) for the whole range of horizontal slownesses, including the almost perfect prediction of the important zero-crossing point. To obtain a good fit at small values of horizontal slowness it was necessary to apply the reciprocity principle to simulate a split-spread geometry. A straight plane-wave decomposition of marine data (in which data from the other side of the source is absent) would generate amplitude values at vertical incidence with half the theoretical value.
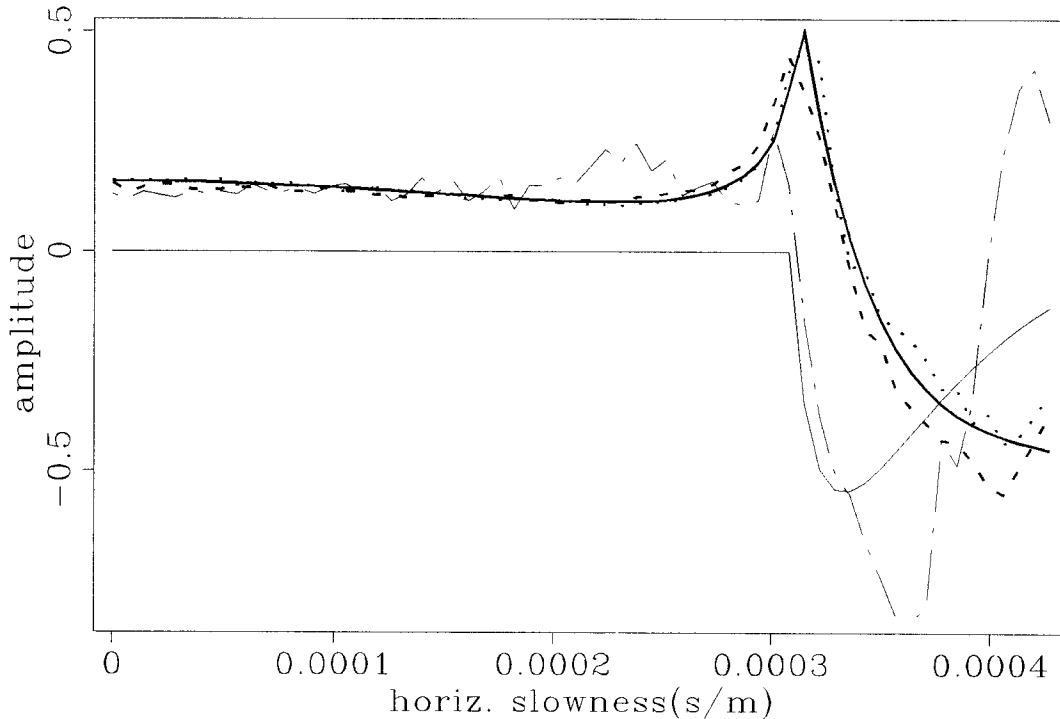

FIG. 3.17. Amplitude versus horizontal slowness of the PP reflection from the interface between the second and third layer of the model. These curves were extracted from the plane-wave decomposition of the wavefields generated by the three modeling schemes. The **thick continuous** line and the **thin continuous** line correspond, respectively, to the real and imaginary parts of the theoretical PP plane-wave reflection coefficient; the **dotted**-line is the amplitude response from the propagator-matrix scheme; the **dashed**-line is the amplitude response from the dual-operator scheme; the **thin dot-dashed**-line comes from the traditional finite-difference scheme.

3.5 Examples

To illustrate the stability of the method in more general cases, a wavefield simulation is performed using a structurally complex transverse-isotropic model, which also includes a water layer with an irregular bottom interface as its first layer. The resulting elastic wavefield cubes $[u_z(x, z, t), u_x(x, z, t)]$ are shown in Figures 3.18 and 3.19. The panel at the top of these figures corresponds to a conventional surface seismic shot gather and the side panel corresponds to a conventional vertical seismic profile (VSP) survey. The set of front panels corresponding to the snapshots of the wave propagation through the earth are what the reflection seismologist must uncover using the information contained in the other two panels.
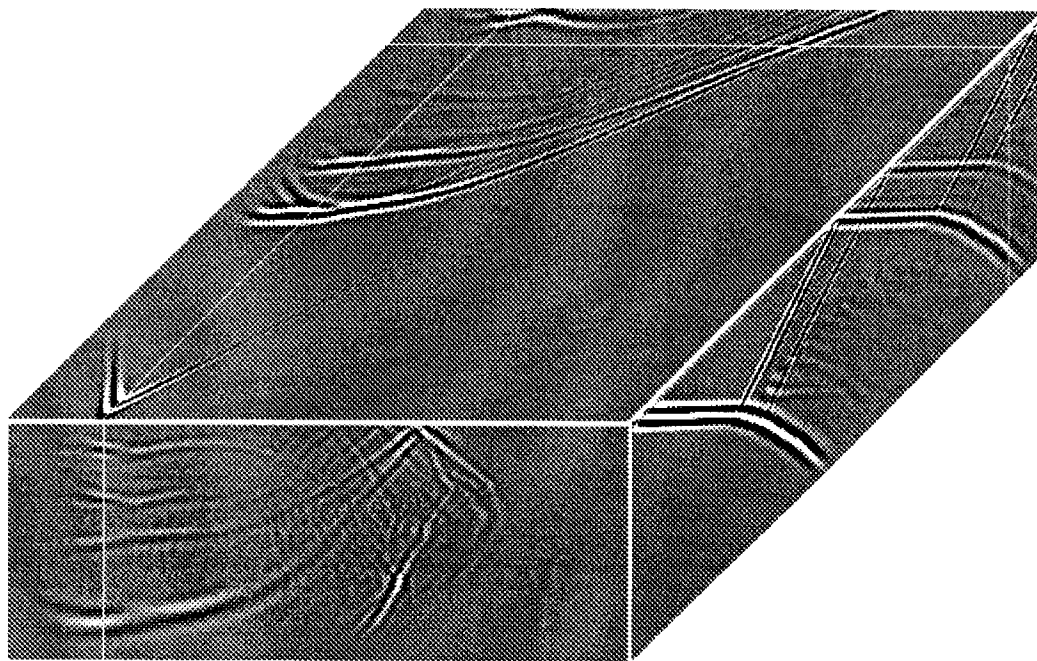

FIG. 3.18. Vertical component of an elastic wavefield simulated with the dual-operator scheme for a structurally complex geologic model. The front panel corresponds to a snapshot of the vertical plane (model space), the top panel is the x-t plane, and the side panel is the z-t plane.
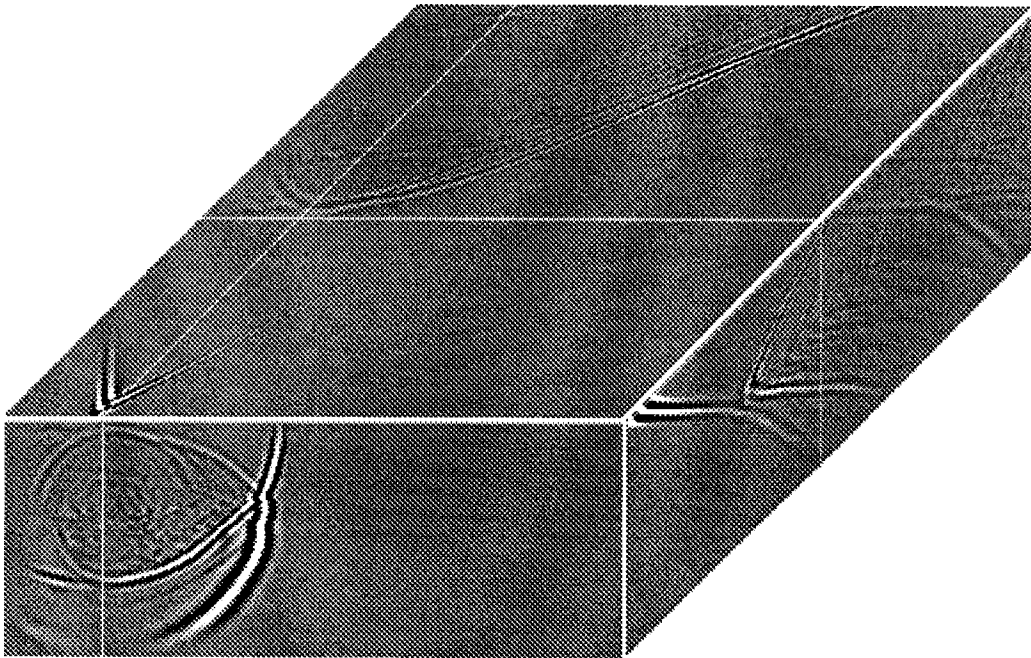
FIG. 3.19. Horizontal component of an elastic wavefield simulated with the dual-operator scheme for a structurally complex geologic model. The front panel corresponds to a snapshot of the vertical plane (model space), the top panel is the x-t plane, and the side panel is the z-t plane. The front panel shows an earlier time frame than the one displayed for the vertical component.

3.6 Summary

Traditional approaches to finite-difference elastic modeling make no distinction between model and wavefield variables. A single differential operator (either in the space or spatial-frequency domain) is used to calculate the spatial derivatives of both the stiffness components and the wavefield components. This lack of distinction can be in part attributed to the way in which most conventional schemes are implemented; the derivatives of the stiffness components are only implicitly computed when the derivatives of the stress components are evaluated.

When the model parameters are a smooth function of the spatial variables, the same high-order, long operator can be used for both model and wavefield variables, but in more realistic cases, when sharp boundaries are present, a short operator should be used for the model parameters. This approach, referred to as the dual-operator method, was implemented in a modified staggered grid within the framework of the equivalent media theory. Tests performed in a simple model that includes a liquid layer show that the method gives less dispersive and more accurate results than the traditional finite-difference method. The angle-dependent, plane-wave response obtained with the dual-operator scheme in that model is more accurate than the one obtained with traditional finite-difference schemes and has similar accuracy to the response obtained with the propagator-matrix scheme implemented here.